CrossMark

Facile synthesis, morphology and structure of Dy_2O_3 nanoparticles through electrochemical precipitation

Taher Yousefi*, Meisam Torab-Mostaedi, Abolfazl Aghaei, Hossein Ghasemi-Mobtaker

Abstract The aim of this research was to introduce a new, facile and simple method for synthesis of Dy_2O_3 nanostructures at room temperature. For the first time, galvanostatic electrodeposition was used to synthesize Dy_2O_3 particles, and the influence of the current density on the structure and morphology of the product was studied. The samples were characterized by X-ray diffraction (XRD), transmission electron microscopy (TEM) and Brunauer–Emmett–Teller (BET). The results show that the current density has little effect on the chemical composition but great effect on the structure and morphology of the samples. The average size of the particles decreases as the applied current density increases. The grain size of as-prepared samples decreases from 500 to 70 nm when the current density increases from 0.5 to 6.0 mA·cm^{-2}. To obtain oxide product, the as-prepared samples were heat-treated at 1,000 °C. The results show that the heat-treated samples have smaller particles. The XRD results show that the similar patterns are observed in the samples synthesized at different current densities, and the only difference from the JCPDS card is the ratio of peak intensities. With the increase in the current density, a decrease in the current efficiency is observed.

Keywords Dy_2O_3; Nanoparticle; Electrodeposition; Nanostructures; Rare earth

T. Yousefi*, M. Torab-Mostaedi, A. Aghaei, H. Ghasemi-Mobtaker
Nuclear Fuel Cycle Research School, Nuclear Science and Technology Research Institute, 14395-836 Tehran, Iran
e-mail: taher_yosefy@yahoo.com

1 Introduction

Owing to 4f electrons, rare earth elements have specific chemical, electronic and optical characteristics, which make them suitable to be used in high-performance luminescent devices and catalyst formulations (such as petrochemical products, refining and treatment of exhaust gases from the mobile sources) [1]. They were also used in high-efficiency phosphors and magnetic to dielectric formulations in the production of ceramic capacitors and superconductors (specially, dysprosium oxide with the cubic structure) [2]. Furthermore, dysprosium has some specific uses which make it as an important rare earth element in various industries. Dysprosium oxide crystallizes as a cubic structure below 1,870 °C. At higher temperatures, it has monoclinic or hexagonal structures. It is highly insoluble and thermally stable. It can be used as either magnetic resonance or optical imaging agents. It has the highest magnetic moments in lanthanide ion, so nanosize dysprosium is a good candidate in T_2 magnetic resonance (MR) imaging [3]. It was proposed to use dysprosium oxide admixed and pelletized with Zr_2O_3 in the advanced heavy-water reactor (AHWR) to maintain the negative void coefficient in the reactor and also to slow down the fast neutrons [4]. In the above-mentioned application and many others, particles with nanosize enhanced the physical and chemical properties compared with bulk materials. This is because of locating high proportion of atoms at their surface. Such nanosize materials can be synthesized by various methods such as precipitation, hydrothermal, spray method and reverse micellar system [1, 5–9].

Precipitation, thermal decomposition and sol–gel are the most studied methods. An example for the precipitation method is homogenous precipitation by urea. Particle growth in the process was described by the short nucleation

Springer

time model of LaMer. In this model, the formation of nuclei is at super-saturation point, and then, nuclei will grow to form larger particles by the addition of solute species. But later, aggregation mechanism was used to describe the process of homogeneous precipitation by urea [10–12]. Several parameters controlling the size and size distribution in this method should be adjusted carefully to have the desirable size and distribution (such as aging time, concentration, temperature, etc.). These parameters will have great effect on the reproducibility of the method. Consequently, the method may practically go out of control.

Thermal decomposition of various inorganic dysprosium precursors in air or nitrogen atmosphere at very high temperatures is another way to produce Dy_2O_3 nanoprticles. $Dy_2(C_2O_4)_3 \cdot 5H_2O$, $Dy(CH_3COO)_3 \cdot 5H_2O$, $Dy(NO_3)_3$ and $Dy_2(OH)_2(CO_3)_2 \cdot 2H_2O$ are some precursors used to prepare Dy_2O_3. But high temperatures used in this process lead to high degree of agglomeration which results in large particles [13].

In sol–gel method, an organic compound of dysprosium such as dysprosium n-butoxide (DB) was dissolved in organic solvent and the sol was formed by hydrolysis of the DB precursor. The gel was obtained by aging at a proper temperature, and then it was calcined to remove the organic components. However, the method would produce narrow distribution of dysprosium oxide nanoparticles, but the precursors were expensive and also the process was time consuming [13, 14]. Electrodeposition, a powerful and interesting process, can be applied in numerous fields [15]. The cathodic electrodeposition of Dy_2O_3 by electro-generation of base was rarely investigated and so it is an interesting subject to be studied. Here, the preparation of Dy_2O_3 nanoparticles via cathodic electrodeposition method was reported.

2 Experimental
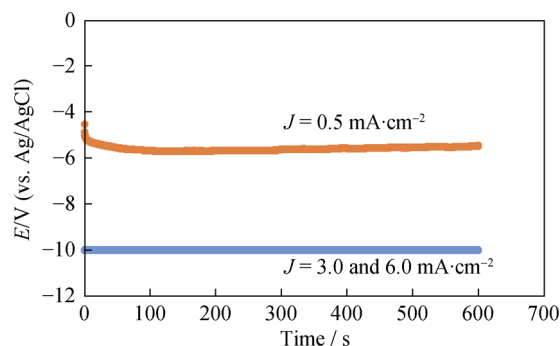
All chemicals were used as received without further purification. $Dy(NO_3)_3$ was purchased from Merck company. Steel plates (316 L) with size of 20.0 nm × 20.0 nm × 0.5 mm were used as the cathode substrate. Before deposition, the steel plates were cleaned by abrasive papers and subsequently washed with diluted hydrochloric acid and distilled water. In the electrochemical cell for deposition, the steel cathode was centered between the two parallel graphite anodes. The electrodeposition was carried out by applying constant current density (0.5, 3.0 and 6.0 mA·cm^{-2}) for 600 s. Thermal annealing was conducted in air between the room temperature and 700 °C at heating rate of 10 °C·min^{-1}. The X-ray diffraction (XRD) powder patterns were obtained on a STOE Model STADI MP diffractometer. The X-ray was generated by a tube with radiation of Cu Kα (0.154 nm). The operational settings for

the XRD scans were: voltage of 40 kV, current of 30 mA and scan range of 3°–100°. The morphologies were measured by transmission electron microscopy (TEM, Phillips EM 2085). The specific surface area for the prepared sample was obtained through measuring N_2 adsorption–desorption isotherms at 77 K with Quanta-chrome NOVA-2200e system.

3 Results and discussion

3.1 Deposition mechanism

Figure 1 shows the curves of potential versus time recorded during galvanostatc deposition of the samples in 0.005 mol·L^{-1} $Dy(NO_3)_3 \cdot 6H_2O$ solution. The change of the shape of the polarization curves with the applied current densities can be related to the reduction reactions at the electrode [16]. The change of shape of polarization curves only at low current density (<1 mA·cm^{-2}) and concentrated electrolyte can be seen clearly in the initial stage of electrodeposition. The transient curves of potential versus time were characterized by the relaxation of cathodic deposition potential toward a constant value. The value of the stabilized cathodic deposition potential decreases toward more negative values as the applied current density becomes more negative as seen in Fig. 1. A continuous variation of potential with time is typically ascribed to a single reaction, whereas sudden changes are the indication of a change in the main reaction occurring at the electrode. Under the applied current density, the potential can be sustained by the following reduction processes:

$$2H_2O + 2e^- \rightarrow H_2 + 2OH^- \tag{1}$$

$$2H_3O^+ + 2e^- \rightarrow H_2 + 2H_2O \tag{2}$$

$$O_2 + 2H_2O + 4e^- \rightarrow 4OH^- \tag{3}$$

Fig. 1 Potential versus time for deposition at 0.5, 3.0 and 6.0 mA·cm^{-2} from 0.005 mol·L^{-1} concentrations of $Dy(NO_3)_3 \cdot 6H_2O$ solutions

$$O_2 + 2H_2O + 2e^- \rightarrow 2OH^- + H_2O_2 \qquad (4)$$

$$NO_3^- + H_2O + 2e^- \rightarrow NO_2^- + 2OH^- \qquad (5)$$
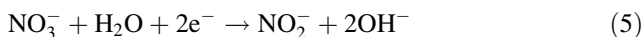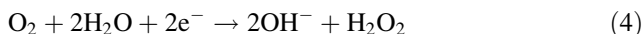
As shown, all these half-cell reactions produce OH$^-$ and cause the increase in pH at the cathode surface (Fig. 2). The reduction in nitrates and oxygen species has a minor role in increasing pH due to the great number of solvent molecules (water) in media. Therefore, the role of the reduction in nitrates and oxygen can be disregarded. The electro-generation of the base at the interface increases the local pH and can lead to the development of dysprosium hydroxide Dy(OH)$_3$ according to the following reaction:

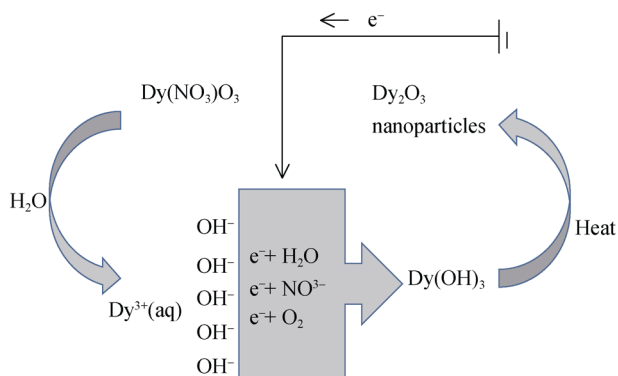$$Dy^{3+} + 3OH^- \rightarrow Dy(OH)_3 \qquad (6)$$
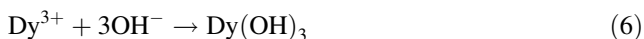
In summary, in cathodic deposition technique, hydrolysis reactions result in the accumulation of colloidal particles near the electrode and the formation of a deposit is caused by flocculation introduced by the electrolyte. The deposit forming on electrode surface can be explained by DLVO (Derjaguin, Landau, Verwey and Overbeek) theory [17]. The DLVO theory states that the total pair interaction between colloidal particles consists of two parts: the columbic double-layer repulsion and van der Waals' attraction. The total energy (E_T) of interaction of two isolated and identically charged particles is defined as:

$$E_T = E_A + E_R \qquad (7)$$

where E_A is attractive energy, and E_R is the repulsive energy. The attractive energy (E_A) of the London-van der Waals' interaction between the two spherical particles can be expressed by:

$$E_A = -\frac{A}{6}\left(\frac{2}{s^2-4} + \frac{2}{s^2} + \ln\frac{s^2-4}{s^2}\right) \qquad (8)$$

where A is the Hamaker constant and $s = 2 + H/a$ (where H is the shortest distance between the two spheres, and a is

the particle radius). If $H \ll a$, Eq. (2) can be simplified in the following formula:

$$E_A = -A\frac{a}{12H} \qquad (9)$$

The repulsive energy (E_R) is:

$$E_R = 2\pi\varepsilon\varepsilon_0 a\psi^2 \ln(1 + e^{-kH}) \qquad (10)$$

where ε is the dielectric constant of the solvent, ε_0 is the vacuum dielectric permittivity, ψ is the surface potential, and $1/k$ is the Debye length:

$$k = \left(\frac{e_0^2 \sum n_i z_i^2}{\varepsilon\varepsilon_0' k'T}\right)^{1/2} \qquad (11)$$

where ε_0' is the electron charge, k' is the Boltzmann constant, T is the absolute temperature, and n_i is the concentration of ions with valence z_i. The repulsion between colloidal particles is directly related to the diffuse layer charge on the particles.

When the diffuse layer repulsion is sufficiently high compared with the van der Waals' attraction, the total energy of particle interaction exhibits the maximum value. This is the energy barrier to particle coagulation.

The DLVO theory explains the existence of critical electrolyte concentration (flocculation value) for coagulation which decreases with the valence of the electrolyte ions of a charge opposite to that of the colloidal particles. As the electrolyte concentration increases, the energy barrier disappears, and coagulation becomes possible (in other words, with the progress of electrodeposition process, the electrolyte concentration near the electrode surface will increase and coagulation will take place).

3.2 Current efficiencies

The cathodic current efficiencies were calculated on the basis of the mass of the deposit and the coulometric data. As shown in Fig. 3, with the increase in current density, the efficiencies decrease. This result is inconsistent with

**Fig. 2** Formation mechanism of Dy$_2$O$_3$ nanoparticles by galvano static technic
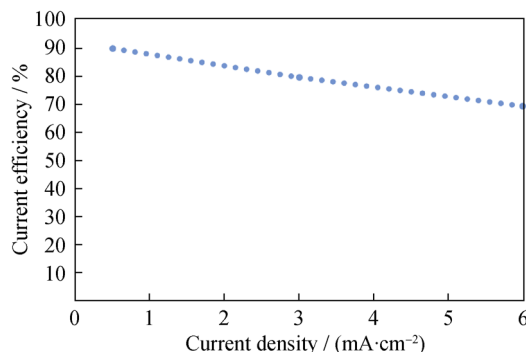
Fig. 3 Current efficiency versus current density

Faraday's law, according to which the deposit weight is proportional to the passed charge. The possible reasons for the deviation of experimental deposit weights from the Faraday's law are clear. When the possible factors that can influence the deposition rate are considered, it seems most reasonable to conclude that such deposit weight behavior is attributed to the low concentration of the electrolyte used for the electrodeposition [18]. Indeed, for electrolytes with low concentration, the rate of cathodic reactions depends on the rate of diffusion of the reacting species, detracting from the deposition process efficiency. Another reasonable factor for the deviation from Faraday's law can be described on the basis of hydrogen evolution at electrode surface. The limitation of the rate of dysprosium ion diffusion toward the cathode surface with current density increasing leads to the subsequent decrease in efficiency. With the increase in current density, the rate of hydrogen evolution increases, and the hydrogen bubbles limit the dysprosium diffusion rate toward the electrode surface. Also, the hydrogen bubbling at the electrode surface would cause the deposit to splash into solution and reduce product on the electrode surface; high current density leads to high rate hydrogen evolution and more splashing.

3.3 Morphologies

The surface morphologies of the sample were investigated by TEM with different applied current densities. Figure 4 shows the TEM images of as-deposited samples at the current densities of 0.5, 3.0 and 6.0 mA·cm^{-2}, respectively. It can be clearly seen that the surface morphology of the samples is significantly affected by the applied current density. As shown in Fig. 4, the decrease in the particle size with the increase in current density is clearly evident.

The morphologies seem to result from the competition between nucleation and growth process at the electrode surface during electro-base generation. At high current density, an instantaneous nucleation mode is favorable and the rate of nucleation is very fast in comparison with the rate of crystal growth [19]. Nuclei form within a very short time, so the coverage rate of electrode surface sites by hydroxide deposition should be very fast. Particles with low growth and small size are hence preferable. In addition, at low current density such as 0.5 mA·cm^{-2}, a particle growth process is preferred, because the rate of crystal growth is higher than that of nucleation, and the nuclei continuously form as the crystals grow. Therefore, thick particles are obtained. A similar finding was reported by Eliaz and Eliyahu [19]. The cathodic deposition of hydroxides/oxide involves an electrochemical reduction step (i.e., H_2O reduction) followed by a chemical precipitation step (i.e., $Dy(OH)_3$ formation); the influence of the chemical precipitation kinetics on the microstructures of
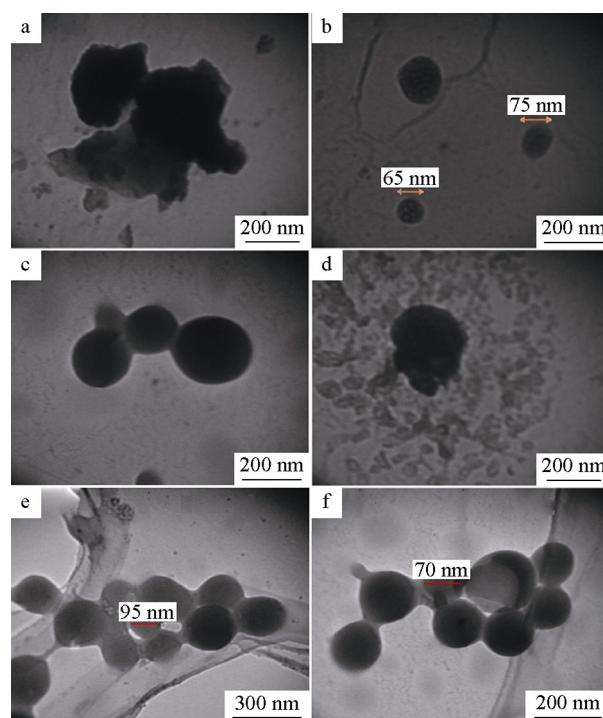
Fig. 4 TEM images of as-deposited samples at **a** 0.5 mA·cm^{-2}, **b** 3.0 mA·cm^2, **c** 6.0 mA·cm^2 for 10 min in water Dy(III) nitrate solution and annealed samples at 1,000 °C at **d** 0.5 mA·cm^2, **e** 3.0 mA·cm^2, **f** 6.0 mA·cm^2

deposits is acceptable. The heat treatment at 1,000 °C causes the decrease in particle size (Table 1), which can be attributed to the liberation of electrolyte ions, water and oxygen molecules from the as-prepared sample at high temperature.

3.4 XRD results

Figure 5 shows the XRD pattern of the samples obtained at different current densities. The as-prepared sample is found to be amorphous (inset in Fig. 5), and at 1,000 °C, the samples display well-defined peaks. The peaks of dysprosium oxide observed in this pattern are based on ICSD No. 061269. It has cubic structure with space group *Ia*-3 (lattice constant of cubic unit cell: 1.0670 nm). The curve at 0.5 mA·cm^{-2} has sharp peaks with high intensity, which shows that the sample has high crystallinity and the particle sizes are not very small. The Scherrer equations [20] for the estimation of particle size are used:

$$D_{hkl} = 0.89\lambda / \beta_{hkl} \cos\theta \tag{12}$$

$$\beta_{hkl} = \Delta 2\theta \pi / 180° \tag{13}$$

where D_{hkl} denotes the average crystal size, λ is the wavelength of the incident X-rays (0.15406 nm), θ is the diffraction angle, and β_{hkl} is the full width at half maximum (*FWHM*). The results are summarized in Table 1. For

Table 1 Particle size of samples

Current density/ (mA·cm^{-2})	FWHM/(°)	Particles size/nm		
		Samples annealed at 1,000 °C (XRD)	As-prepared samples (TEM)	Samples annealed at 1000 °C (TEM)
0.5	0.2509	70	500	150
3.0	0.4723	55	210	95
6.0	0.2804	30	65	70
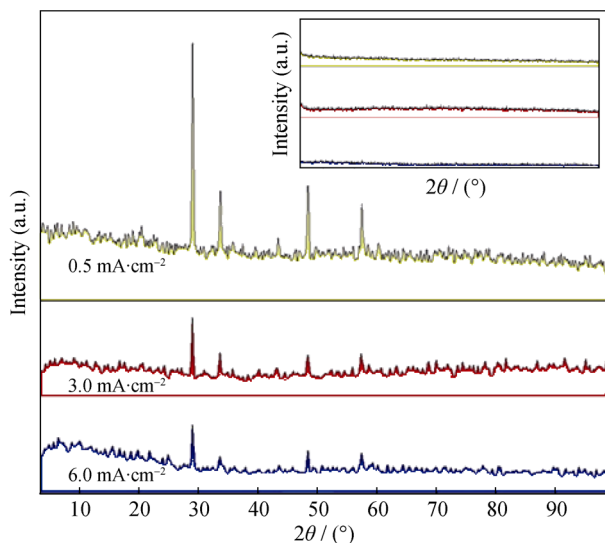
Fig. 5 XRD patterns of sample synthesized at 6.0, 3.0 and 0.5 mA·cm^{-2} and annealed at 1,000 °C. Insert being XRD patterns of as-prepared samples

curves at 3.0 and 6.0 mA·cm^{-2}, the peak intensities are low, which can be concluded that the particles are smaller than those of previous sample. The particle size calculated in these samples is 27.8 nm based on Scherrer equation. The areas of the curves show the formation of amorphous phase in these samples.
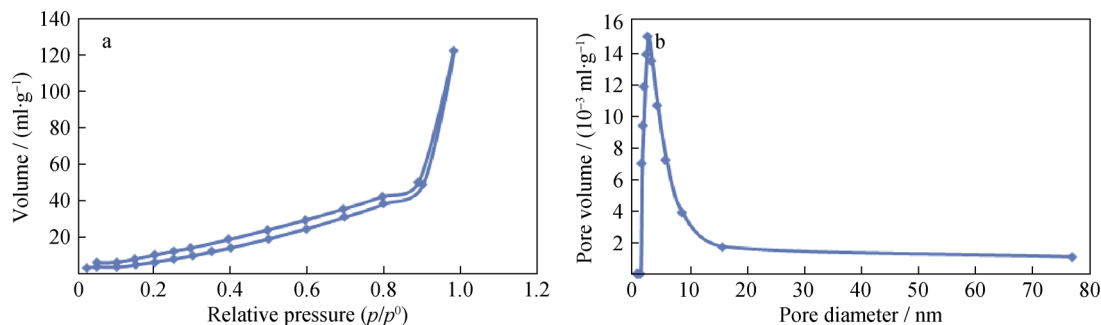
The crystal size estimated from XRD Scherrer's equation is slightly smaller than that estimated from TEM. This is because XRD gives the information of crystalline region only, and the amorphous region does not contribute to this process. Moreover, TEM gives the complete images of the nanoparticles.

3.5 BET results

For the determination of the specific surface area, the pore size distribution and the pore volume, the sample with the smallest particle sizes was selected (synthesized at 6 mA). An adsorption isotherm is obtained by measuring the amount of gas adsorbed within a wide range of relative pressures at constant temperature (typically liquid N$_2$, 77 K). Conversely, desorption isotherms are achieved by measuring the gas removed as the pressure reduces. The surface area of sample annealed at 1,000 °C and synthesized at 6 mA·cm^{-2} (sample with the smallest particle size) was measured using the Brunauer–Emmett–Teller (BET) method. The N$_2$ adsorption–desorption isotherm and BJH pore size distribution by Barrett–Joyner–Halenda (BJH) method at 77 K are shown in Fig. 6. Before adsorption measurements, the sample was activated by heating to 423 K at heating rate of 0.5 K·min^{-1} and keeping at this temperature under the turbo molecular pump vacuum. The amount of N$_2$ adsorbed at p/p^0 of 0.995 is 125 cm^3·g^{-1}. The isotherm has Type III form that is characterized by the heat of adsorption, less than the heat of liquification for adsorbate; adsorption proceeds as the adsorbate interaction with the adsorbed layer is greater than the interaction with the adsorbent surface, and the nitrogen hysteresis loop is Type H3 according to the International Union of Pure and Applied Chemistry (IUPAC) classification [21], which indicates the existence of slit-shaped pores between the crystallites. The BET surface area of the sample is found to be 91 m^2·g^{-1}. The pore size distribution of Dy$_2$O$_3$ is shown in Fig. 6b. According to IUPAC nomenclature, the size of micropores is <2 nm in diameter, that of mesopores is

Fig. 6 N$_2$ adsorption (down curve)-desorption (up curve) isotherms **a** and BJH pore size distribution curve **b** of sample synthesized at 6 mA·cm^{-2}

between 2 and 50 nm in diameter, and that of macropores are >50 nm in diameter. For our sample, a narrow peak with mean pore widths of around 6 nm emerges, indicating that the sample contains micropores.

4 Conclusion

Dy_2O_3 powders were produced by electrochemical deposition. The growth of the nanostructures was associated with the precipitation of $Dy(OH)_3$ induced by the increase in pH on the cathode surface caused by the reduction processes. Owing to low concentration compared with water molecules, it seems that the reduction in the dissolved oxygen and nitrates ions do not increase the interfacial pH sufficiently, which is necessary to form colloidal $Dy(OH)_3$ particles. The size variation of Dy_2O_3 as a function of current density was studied. The cathodic current density varies from 0.5 to 6.0 mA·cm^{-2}. The result shows that the morphology is markedly affected by current density and as the cathodic current density increases, the mean nanocrystal size decreases. The amount of the deposited material (current efficiency) as a function of current density was studied. The results show that with the increase in the current density, the efficiencies decrease; consequently, a significant deviation from Faraday's law can be observed. This behavior is attributed to the low concentration of the electrolyte used for the electrodeposition and hydrogen bubbling at the electrode surface.

References

[1] Wang G, Wang Z, Zhang Y, Fei G, Zhang L. Controlled synthesis and characterization of large-scale, uniform $Dy(OH)_3$ and Dy_2O_3 single-crystal nanorods by a hydrothermal method. Nanotechnology. 2004;15(9):1307.

[2] Rao RP. Tb^{3+} activated green phosphors for plasma display panel applications. J Electrochem Soc. 2003;150(8):H165.

[3] Kattel K, Park JY, Xu W, Kim HG, Lee EJ, Bony BA, Heo WC, Jin S, Baeck JS, Chang Y, Kim TJ, Bae JE, Chae KS, Lee GH. Paramagnetic dysprosium oxide nanoparticles and dysprosium hydroxide nanorods as T_2 MRI contrast agents. Biomaterials. 2012;33(11):3254.

[4] Singh DK, Kotekar MK, Singh H. Development of a solvent extraction process for production of nuclear grade dysprosium oxide from a crude concentrate. Desalination. 2008;232(1–3):49.

[5] Happy, Tok AIY, Su LT, Boey FYC, Ng SH. Homogeneous precipitation of Dy_2O_3 nanoparticles—effects of synthesis parameters. J Nanosci Nanotechnol. 2007;7(3):907.

[6] Wang LS, Zhou YH, Quan ZW, Lin J. Formation mechanisms and morphology dependent luminescence properties of Y_2O_3: Eu phosphors prepared by spray pyrolysis process. Mater Lett. 2005;59(10):1130.

[7] Sohn JR, Kang YC, Park HD. Morphological control of Y_2O_3: Eu phosphor particles by adding polymeric precursors in spray pyrolysis. Jpn J Appl Phys. 2002;41(1):3006.

[8] Hirai T, Asada Y, Komasawa I. Preparation of Y_2O_3: Eu^{3+} nanoparticles in reverse micellar systems and their photoluminescence properties. J Colloid Interface Sci. 2004;276(2):339.

[9] Lee MH, Oh SG, Yi SC. Preparation of Eu-doped Y_2O_3 luminescent nanoparticles in nonionic reverse microemulsions. J Colloid Interface Sci. 2000;226(2):65.

[10] Matijevic E, Hsu WP. Preparation and properties of monodispersed colloidal particles of lanthanide compounds: I. Gadolinium, europium, terbium, samarium, and cerium(III). J Colloid Interface Sci. 1987;118(2):506.

[11] LaMer VK, Dinegar RH. Theory, production and mechanism of formation of monodispersed hydrosols. J Am Chem Soc. 1950;72:4847.

[12] Jeevanandam P, Koltypin Y, Palchik O, Gedanken A. Synthesis of morphologically controlled lanthanum carbonate particles using ultrasound irradiation. J Mater Chem. 2001;11(3):869.

[13] Sreethawong T, Chavadej S, Ngamsinlapasathian S, Yoshikawa S. A simple route utilizing surfactant-assisted templating sol–gel process for synthesis of mesoporous Dy_2O_3 nanocrystal. J Colloid Interface Sci. 2006;300(1):219.

[14] Farooq MH, Yang HL, Xu XG, Ran CJ, Miao J, Rafique MY, Pan LQ, Jiang Y. Room temperature ferromagnetism of Si-doped ZnO thin films prepared by sol–gel method. Rare Met. 2013;32(2):165.

[15] Yang ML. Potentiostatic deposition of differently shaped Pt and PtBi nanoparticles. Rare Met. 2013;32(4):375.

[16] Creus J, Brezault F, Rébéré C, Gadouleau M. Synthesis and characterization of thin cerium oxide coatings elaborated by cathodic electrolytic deposition on steel substrate. Surf Coat Technol. 2006;200(14–15):4636.

[17] Zhitomirsky I. New developments in electrolytic deposition of ceramic films. Am Ceram Soc Bull. 2000;79:57.

[18] Gal-Or L, Silberman I, Chaim R. Electrolytic ZrO_2 coatings. J Electrochem Soc. 1991;138(7):1939.

[19] Eliaz N, Eliyahu M. Electrochemical processes of nucleation and growth of hydroxyapatite on titanium supported by real-time electrochemical atomic force microscopy. J Biomed Mater Res Part A. 2007;80(3):621.

[20] Tok AIY, Boey FYC, Dong Z, Sun XL. Hydrothermal synthesis of CeO_2 nano-particles. J Mater Process Technol. 2007;190(1–3):217.

[21] Rouqureol F, Rouquerol J, Sing K. Adsorption by Powders and Porous Solids. New York: Academic Press; 1980. 18.